Isolation of optomechanical nonlinearities in nanomechanical cantilevers

Westwood-Bachman, Jocelyn N.; Firdous, Tayyaba; Kobryn, Alexander E.; Belov, Miro; Hiebert, Wayne K.

Publisher's version / Version de l'éditeur:
https://doi.org/10.1103/PhysRevA.105.053517
Physical Review A, 105, 5, 2022-05-18

Isolation of Optical Nonlinearities in Nanomechanical Cantilevers

Jocelyn N. Westwood-Bachman and Tayyaba Firdous
Department of Physics, University of Alberta, Edmonton, Alberta, Canada, T6G 2E1. and
Nanotechnology Research Centre, National Research Council Canada,
11421 Saskatchewan Dr NW, Edmonton, Alberta, Canada, T6G 2M9.

Alex Kobryn and Miro Belov
Nanotechnology Research Centre, National Research Council Canada,
11421 Saskatchewan Dr NW, Edmonton, Alberta, Canada, T6G 2M9.

Wayne K. Hiebert*
Nanotechnology Research Centre, National Research Council Canada,
11421 Saskatchewan Dr NW, Edmonton, Alberta, Canada, T6G 2M9. and
Department of Physics, University of Alberta, Edmonton, Alberta, Canada, T6G 2E1.

(Dated: November 1, 2021)

In this paper we study the nonlinearities present in a nano-optomechanical system consisting of a cantilever coupled to a racetrack resonator. We show that higher order harmonics in the mechanical frequency spectrum are indicative of a readout nonlinearity and we connect these harmonics to the optical cavity transmission with detuning function and its derivatives. We also show that there are optical force nonlinearities that cause a Duffing-like response in the driven mechanical signal. The Duffing-like nonlinearity produces a softening effect when the probe laser is blue-detuned, and a stiffening effect when the probe laser is red-detuned. The optical force and readout nonlinearities are difficult to separate using a purely experimental approach. We demonstrate the use of a numerical model of the pump-and-probe system to analyze the nonlinearities independently. The numerical model also allows us to estimate the amplitude of the system, predicting the exact detuning where nonlinearities cancel each other to produce higher critical amplitude, and ultimately giving a mass sensitivity level of 83 yg/Hz$^{1/2}$. The numerical model provides a rich understanding of the complexities of the nano-optomechanical system and is much needed for the development of sensors with increased dynamic range and overall performance.

I. INTRODUCTION

Nonlinear behaviour in optomechanical systems is important for many reasons. If the mechanical device is used as a sensor, nonlinearities are detrimental and much work has been devoted to eliminating or avoiding the nonlinearities in order to increase the dynamic range of the sensors [1–3]. For other applications, such as in quantum optics or oscillator circuits, nonlinearities are essential. For example, it has been shown that mechanical Duffing nonlinearities can help prepare squeezed mechanical states [4], and can also help form autonomous oscillators [5]. Regardless of the application of the nanomechanical device, understanding its nonlinear behaviour is crucial. For these reasons, it is important to understand how the actuation and readout methods can introduce nonlinearities into a nanomechanical system. For some actuation and readout techniques, nonlinearities are well understood. One example is in capacitive transduction, where nonlinear effects due to pull-in are well studied and the effects can be quantified and tuned [6, 7]. When both an actuation and readout is optomechanical, however, nonlinearities in the transduction are not as well explored [8–12]. In optomechanics, the complex interaction between the nanomechanical device and the optical cavity can lead to a wide range of nonlinear effects. In addition to the purely mechanical nonlinearities observed such as stiffening and softening mechanical nonlinearities, such as those seen in transduction of even modes in doubly clamped beams [13], nonlinear coupling between the mechanical device and the optical cavity can be achieved [14], and both radiation pressure force and dispersive optical forces are inherently nonlinear [15, 16]. Nonlinearity is further complicated when two lasers are coupled to the optomechanical system [13, 17–19]. The use of two lasers allows differing actuation and readout strengths with separate control of cavity detuning values (for example, allowing control of optomechanical spring effects for sensing enchancement [17]).

For mass sensing nanomechanical devices, the nonlinearities of most interest are those that limit the dynamic range of the sensor [20]. For doubly clamped beams, this nonlinearity is typically the mechanical Duffing nonlinearity. Cantilevers, however, have a significantly higher threshold for mechanical nonlinearity, since the onset of mechanical nonlinearity is proportional to the length of the cantilever, instead of the thickness [2, 21]. Therefore, the type of nonlinearity that a cantilever will encounter at the peak of its dynamic range in an optomechanical system is much more likely to be from another source, such as optomechanical forces.

In this article, the sources of nonlinearity affecting the

* Wayne.Hiebert@nrc-cnrc.gc.ca

dynamic range of a cantilever that is both actuated and read out optomechanically is explored. We consider the simultaneous effects of both a pump and probe laser on the nonlinear behaviour of a nanomechanical cantilever coupled to a racetrack resonator. Previous work has studied the effects of a single pump laser actuating a nanomechanical cantilever via the optical gradient force [16] or found parametric instability solutions for a single coupled laser [9]. The addition of a second laser, the probe laser, into the system substantially increases the complexity and produces counter-intuitive behaviour. Both the readout nonlinearity and optical force nonlinearities caused by the large amplitude of the cantilever are examined. Readout nonlinearity harmonics are compared analytically in terms of derivatives of the local optical resonance shape as a function of detuning. Combined readout nonlinearity and optical force nonlinearity are treated via numerical modeling based on modifying the nonlinear optomechanical equations of motion from power coupling formalism [22, 23] with the addition of a second laser field. The numerical model shows good agreement with experimental data. Furthermore, by separating the mechanical and optical outputs, the model allows insight into the dynamics of the system even when readout nonlinearities obscure the experimental results. When accounting for varying optomechanical coupling strength, the model also accurately localizes an optimal detuning value for minimizing nonlinearity and maximizing dynamic range producing a mass sensitivity level of 83 yg/Hz$^{1/2}$ for the particular device considered.

The manuscript is presented in sections. The scope of the problem is introduced in Section II where it is conceptualized how large amplitude motions induce optomechanical nonlinearities in both signal transduction and forces. The mathematical background for nonlinear mechanical resonators is recalled in Section III including the connection between nonlinear harmonic oscillator terms and the critical amplitude. In Section IV, we provide details on the fabrication and initial characterization of the optomechanical system. Included is analysis of optical cavity splitting, optical nonlinearity, optomechanical coupling calibration, and the thermomechanical noise floor. In Section V we present the bulk of the results. We begin with the experimental observation that positioning the probe laser on the blue side of the optical cavity results in a softening effect, and that positioning the probe laser on the red side of the cavity results in a stiffening effect. This is directly opposite to what is described in [24, 25] for a typical optomechanical system. We confirm that thermomechanical noise calibration described in [1] does not hold under large amplitudes due to transduction nonlinearity. This readout nonlinearity introduces harmonics into the mechanical frequency spectrum, which we observe experimentally and demonstrate their link to the shape of the optical cavity transmission curve. We then explore in depth the cause of the unexpected stiffening and softening behaviour. To model our pump-and-probe optomechanical system, we derive a numerical model that includes both lasers and can be used to account for the optical force nonlinearity introduced by the probe laser detuning in the optical cavity resonance. We demonstrate that the optical force nonlinearity introduced by the evanescent field decay outside of the waveguide is crucial to include in the numerical model. When including this additional source of nonlinearity, we show that the numerical model can: (i) correctly identify the softening and stiffening behaviour at every detuning, (ii) is able to decouple the mechanical and optical system responses, (iii) can separate the readout and force nonlinearity contributions in the system, and (iv) can report an accurate amplitude of mechanical motion of the mechanical device. The latter is important when the thermomechanical noise calibration is ineffective due to readout nonlinearity. We show an application of the numerical model to locate a detuning with minimum optomechanical force nonlinearity and a corresponding peak in critical amplitude that allows almost a factor of 5 improvement in dynamic range. In Section VI we summarize the results highlighting the three different contributions to the nonlinearity: the readout, the optical cavity force, and the optical evanescent force. We conclude in Section VII.

II. INTRODUCTION TO LARGE AMPLITUDE MOTION OPTOMECHANICAL NONLINEARITIES

The power coupling formalism of optomechanical systems produces coupled differential equations of motion for the optical field and the mechanical displacement (see section V F). These are usually linearized to simplify the system, assuming only small changes to the field amplitude and displacement. However, even in the Doppler regime, large amplitude mechanical motions, through optomechanical coupling, can modify the cavity detuning by a large fraction of the cavity linewidth. In this case, linearization does not accurately represent the system dynamics. This situation is depicted in Fig. 1. The Lorentzian curve in is an idealized generic optical cavity resonance transmission vs detuning. Mechanical motion causes the cavity resonance position to oscillate in wavelength. Alternatively, a fixed optical wavelength interacting with the cavity can be viewed as oscillating with respect to the transmission curve. Consider a detection laser with fixed wavelength set near the maximum slope point on the side of the resonance curve to maximize optomechanical readout signal (shown by the red star). For small mechanical motions, where the cavity oscillates a tiny fraction of its linewidth, the readout signal is proportional to the amplitude via the local slope of the curve in Fig. 1(b). This leads to a well-behaved transduction signal (at a given laser detuning) that allows, for example, calibration using thermomechanical noise and known temperature to assign a displacement axis directly to the signal. On the other hand, for large amplitude motion such that displacement times optomechanical coupling coefficient is comparable to cavity linewidth, the laser samples a large range of cavity detuning values during the oscillation cycle of the mechanics (Fig. 1(c)). For readout, it is clear that the transduction signal becomes nonlinear and full of harmonic content.

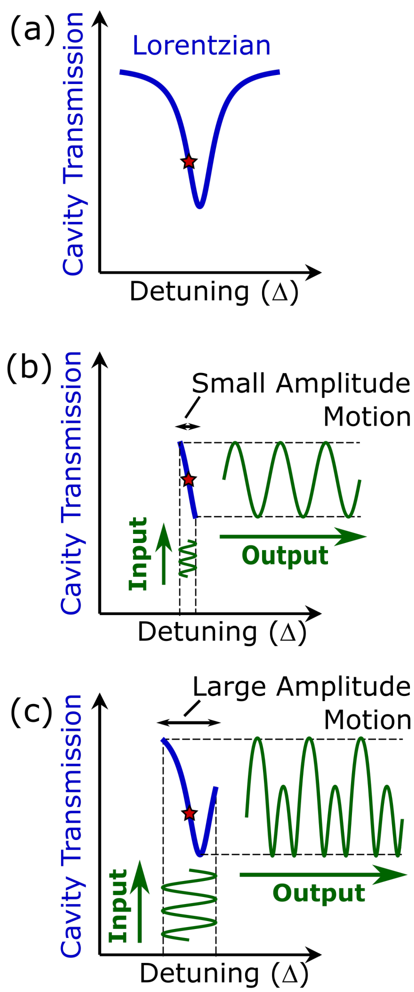

FIG. 1. Concept of mechanical motion induced nonlinearity in large amplitude optomechanical systems. (a) A generic Lorentzian cavity transmission function with respect to optical detuning from cavity resonance is considered. A fixed optical frequency interacts with the cavity, initially located at the red star. The position of the star on the Lorentzian curve changes with mechanical position via optomechanical coupling. (b) For small amplitude motion, the cavity movement under the fixed frequency samples the local function slope. (c) For large amplitude motion (comparable to the cavity linewidth), the output is nonlinear with harmonics. The input in parts (b) and (c) arises from sinusoidal mechanical motion.

On the optomechanical force side, nonlinearity arises from the displacement dependent force in the equation of motion (see section V F) where force depends on cavity field amplitude, which in turn changes substantially over an oscillation cycle for large amplitude motion. Nonlinearity in the equation of motion can be understood via Duffing oscillator analysis, which is recalled in the following section. With two optical frequencies, analytical treatment of the nonlinearity becomes difficult [13]. However, this combination of readout transduction nonlinearity, and force nonlinearity, can be treated numerically by time-step solving the nonlinear coupled equations of motion (section V F).

III. THEORETICAL DESCRIPTION OF NONLINEAR RESONATORS

To determine the upper bound on the dynamic range of a sensor, one experimental approach is to gradually increase the driving power until a nonlinearity is observed. Previous studies have demonstrated that there are several potential sources of nonlinearity for nanomechanical resonators. In the case of cantilevers, the onset of geometric nonlinearity is proportional to the device length according to $a_{\mathrm{cr,mech}} = 6.3 l_{\mathrm{m}}/Q^{1/2}$ [2]. Using this relation, the mechanical critical amplitude for the cantilever measured here, with a length of 2.89 μm, is expected to be approximately 180 nm. This amplitude is double the size of the gap between the cantilever and the waveguide and therefore we reasonably expect that another source of nonlinearity will occur before the mechanical nonlinearity is reached. Our goal with these measurements is to find the onset of nonlinearity, and to determine the source of this nonlinearity. Once we know the source of the nonlinearity, we may be able to design future devices with higher linear ranges to improve the performance of the mass sensing devices. Other potential sources of nonlinearity include actuation nonlinearity, which has been observed in cantilevers under electrostatic actuation [6, 26]. This type of nonlinearity affects the amplitude that can be attained with a given actuation method. Another type of nonlinearity is a readout nonlinearity. This type of nonlinearity can result in a nonlinear relationship between the amplitude of the nanomechanical device and the output signal that is measured [27], but does not affect the actual amplitude of the device.

The behaviour of a nonlinear resonator, regardless of the source of nonlinearity [28], can be described by a differential equation of the damped, driven simple harmonic oscillator. Two additional terms are included in the differential equation to account for the quadratic and cubic nonlinearities, as shown in the following differential equation [16, 29]:

$$m_{\mathrm{eff}} \frac{\mathrm{d}^2 x}{\mathrm{d}t^2} + \frac{m_{\mathrm{eff}}\Omega_0}{Q}\frac{\mathrm{d}x}{\mathrm{d}t} + k_{\mathrm{eff}} x + m_{\mathrm{eff}}\alpha_2 x^2 + m_{\mathrm{eff}}\alpha_3 x^3 = F(t), \quad (1)$$

where x is the amplitude of the mechanical device, t is time, m_{eff} is the effective mass, Ω_0 is the fundamental resonance frequency, Q is the mechanical quality factor, k_{eff} is the effective spring constant, α_2 is the second-order or quadratic nonlinearity coefficient, and α_3 is the third-order or cubic nonlinearity coefficient, and $F(t)$ is the displacement independent applied driving force. Any nonlinear and displacement dependent portions of the force (e.g. with dependence on x^2 or x^3) can be lumped into α_2 and α_3. A nonlinear resonator with α_3 as the dominant nonlinearity term is usually referred to as a Duffing resonator. Experimentally, a Duffing resonator has a frequency resonance curve with a shark-fin shape and exhibits bi-stability.

The onset of nonlinearity, called the critical amplitude a_{cr}, is generally considered to be the upper bound on a sensor's dynamic range [7, 16, 20, 21, 30]. The critical amplitude is the point at which the Lorentzian lineshape of the mechanical signal begins to exhibit the shark-fin shape. Mathematically, this can be described as $\mathrm{d}^2\Omega/(\mathrm{d}B_{\mathrm{NL}}^2)^2 = 0$, where B_{NL} is the frequency-dependent nonlinear amplitude of the resonator. The critical amplitude is described as [29]

$$a_{\mathrm{cr}} = \left(\frac{8\Omega_0^2}{3\sqrt{3}Q\alpha}\right)^{1/2}, \tag{2}$$

where α is the combined quadratic and cubic nonlinearity terms. To combine the two nonlinearity terms into a single term describing the nonlinearity of the resonator, we can use the expression [31]:

$$\alpha = \alpha_3 - 10\alpha_2^2/9\Omega_0^2. \tag{3}$$

The critical amplitude can be calculated as if the total nonlinearity is known. For optomechanical nonlinearities, force dependence on optical field amplitude and detuning Δ (cf. Eq. 8) shows up inside α, thus Eq. (2) gives a detuning-dependent critical amplitude.

The experimental procedure for determining the critical amplitude is to increase the drive power linearly, and record the peak amplitude and frequency of the mechanical device. The results of this experiment produce a plot of amplitude versus frequency that is often referred to as the "backbone" curve of a nonlinear device. To extract the nonlinearity coefficient from this curve, we use the following expression [29]:

$$a_{\mathrm{peak}} = \sqrt{\frac{8}{3}\frac{\Omega_0(\Omega_{\mathrm{peak}} - \Omega_0)}{\alpha}}, \tag{4}$$

where α is positive for a stiffening nonlinearity and negative for a softening nonlinearity.

With this description of nonlinear resonators in mind, we can begin characterization of the pump-and-probe optomechanical system to determine the sources of nonlinearity and therefore the upper bound on the dynamic range of the device for mass sensing.

IV. OPTOMECHANICAL SYSTEM FABRICATION AND CHARACTERIZATION

The optomechanical system was fabricated on a silicon-on-insulator chip with a 220 nm thick device layer and a 2 μm thick sacrificial oxide layer. The mechanical device has a length of 2.89 μm, which is coupled to an optical racetrack cavity. The cantilever was 220 nm wide and 130 nm thick and the gap between the racetrack resonator and the cantilever was approximately 90 nm. The racetrack resonator had 5 μm radius with a straight coupling section 3 μm long. The waveguides width was 500 nm and the coupling gap between the bus waveguide and the racetrack resonator was 250 nm. Grating couplers were used to couple the incident light into the bus waveguide. The optomechanical system was fabricated at imec. Post-processing to release the devices was completed at the University of Alberta NanoFab. The only post-processing required was a buffered oxide etch to release the cantilever. This was a timed, maskless process to release the narrow waveguides while keeping the waveguides attached to the oxide layer. A scanning electron microscope (SEM) image of the mechanical cantilever device before release is shown in Figure 2.

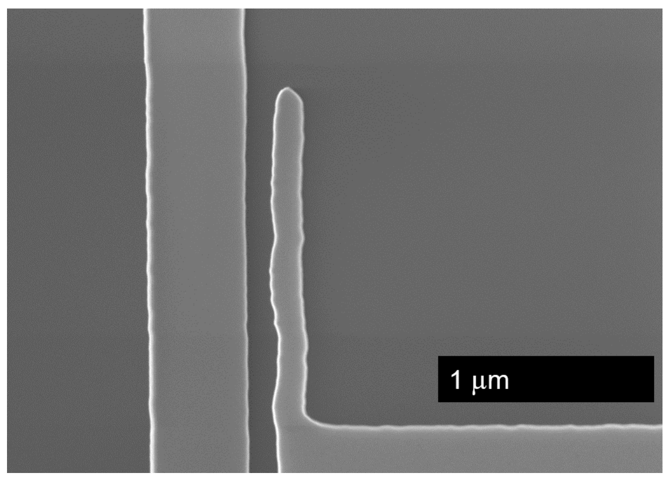

FIG. 2. Scanning electron microscope (SEM) image of the nanomechanical cantilever adjacent to an optical racetrack resonator.

For characterization, we use the free-space confocal microscope setup described in [32]. The DC component of the signal is used to characterize the optical cavity, while the AC component is sent to a digital lock-in amplifier and used to characterize the mechanics of the system. To actuate the devices, we use the optical driving technique. The driving frequency is set by the lock-in amplifier.

First, we characterize the response of the optical racetrack cavity. The pump laser is deactivated and the wavelength of the probe laser is swept to measure the optical response over a wide wavelength range from 1530 nm to 1570 nm, as shown in Figure 3(a). Three optical cavity resonances are observed, with an FSR of approximately

14.5 nm. The first two optical cavity resonances show peak splitting, which is caused by coherent backscattering. For the following experiments, the pump laser is placed at the bottom of the highest wavelength resonance unless otherwise specified. The probe wavelength is positioned on the side of the centre optical cavity, close to 1548 nm.

A fine scan is used to provide detailed information about the blue half of the split optical cavity, as it is the optical cavity used to measure the optomechanical interaction. The scan was first performed at low power, with approximately 77 μW in the bus waveguide (Figure 3(c), blue circles). The response begins at 0 dB on the blue side of the cavity, but does not reach 0 dB on the red side due to the peak splitting effect. The power was then increased to 108 μW (Figure 3(c), red circles). As the power increased, asymmetry in the optical cavity was observed and the optical resonance increased in wavelength.

A. Optical Cavity Model

To model for optical cavity, we first fit the data recorded at low input power using the Eq. (5), the standard power coupling equation for an all-pass microring resonator.

$$T_{\mathrm{ap}} = \left|\frac{s_{\mathrm{t}}}{s_{\mathrm{i}}}\right|^2 = -\frac{\tau - a_{\mathrm{rt}}e^{\phi}}{1-\tau a_{\mathrm{rt}}e^{\phi}}, \tag{5}$$

where τ is transmission coefficient and a_{rt} is one minus the round trip loss. Using the values obtained for τ and a_{rt}, we can develop a model for the nonlinearities in the higher power sweeps. The equation for nonlinear transmission through an all-pass racetrack resonator can be derived using the power coupling formalism [23]. The result of this derivation is the inclusion of a nonlinear phase ϕ_{NL} to Eq. (5), such that the total round trip phase is equal to $\phi+\phi_{\mathrm{NL}}$. However, this equation cannot be used alone to perform a curve fit to the experimental data because the nonlinear phase changes throughout the entire wavelength sweep, depending on the proximity to the optical resonance. To solve for the nonlinear phase at each point in the optical resonance, we use the expression for the nonlinear amplitude inside the optical cavity. By taking the square of the absolute value of the amplitude in the racetrack resonator and simplifying the result we obtain the following expression [23]:

$$\frac{1}{1+F\sin^2(\frac{\phi+\phi_{\mathrm{NL}}}{2})} = -\frac{c\phi_{\mathrm{NL}}n_{\mathrm{eff}}^2A_{\mathrm{eff}}}{n^2n_2\omega P_{\max}L_{\mathrm{eff}}}, \tag{6}$$

where F is the contrast of the racetrack resonator and is defined as $F = 4\tau a_{\mathrm{rt}}/(1-\tau a_{\mathrm{rt}})^2$ for a racetrack in the all-pass configuration, τ and a_{rt} are defined above, n is the bulk index of the silicon and is equal to 3.45, n_2 is the nonlinear index of the silicon waveguides, $P_{\max}$ is the peak power inside the racetrack on resonance, and A_{eff} is the effective modal area of the waveguide. Both n_{eff} and A_{eff} can be obtained using commercial mode solver software (Lumerical) [33]. Finally, $L_{\mathrm{eff}} = (1-e^{-\alpha_0 L_{\mathrm{c}}})/\alpha_0$ is the effective length of the racetrack resonator, which accounts for the optical loss of the waveguide α_0 in units of 1/m, and L_{c} is the physical cavity length. All of these parameters are known or can be solved for using simulation, with the exception of n_2. This nonlinear index describes how the effective index of the waveguide changes as a function of intensity. This parameter is not known for this specific racetrack resonator configuration. Although it is possible to measure this value experimentally [34], it is sufficient in our case to use this value to tune the nonlinear index. Essentially, we can use n_2 as a free parameter, and vary it to produce a range of nonlinear phase shifts from Eq. (6). Then the nonlinear phase is substituted back into Eq. (5) to produce a model of the optical transmission. To determine the correct value for n_2, we extract the wavelength shift observed when the power is increased from 77 μW to 108 μW from the experimental data. We can then adjust n_2 in the model until the correct shift is observed between the curve fit to the 77 μW data and the model. The model for the higher power data is shown in Figure 3. Although this model is not a curve fit, it does provide a good estimate of the curve shape. The properties of the probe and pump optical resonances are summarized in Tables I, II, and III. The probe laser is maintained below the experimentally determined threshold value of 0.23 mW for self-oscillation. The pump laser is always positioned at zero detuning to avoid introducing self-oscillation. The amplitude in the ring is dependent on the overall loss rate γ, the external loss rate associated with coupling γ_{ex}, the power in the bus waveguide P_{bus}, and the detuning $\Delta = \omega - \omega_0$. The optomechanical coupling coefficient G describes the interaction of the optical cavity with the nanomechanical device.

TABLE I. List of probe optical cavity properties ($\lambda \approx$ 1548 nm)

Parameter	Value	Unit
a_{rt}	0.9977	-
τ	0.9952	-
$\gamma/2\pi$	2.04	GHz
$\gamma_{\mathrm{ex}}/2\pi$	1.37	GHz
P_{bus}	107.8	μW
$\omega_0/2\pi$	193.8	THz

B. Optomechanical Properties of the System

Once the optical cavity parameters have been determined, the mechanical properties of the system can be studied. Based on the dimensions observed in the SEM image in Figure 2, we can calculate the effective mass of

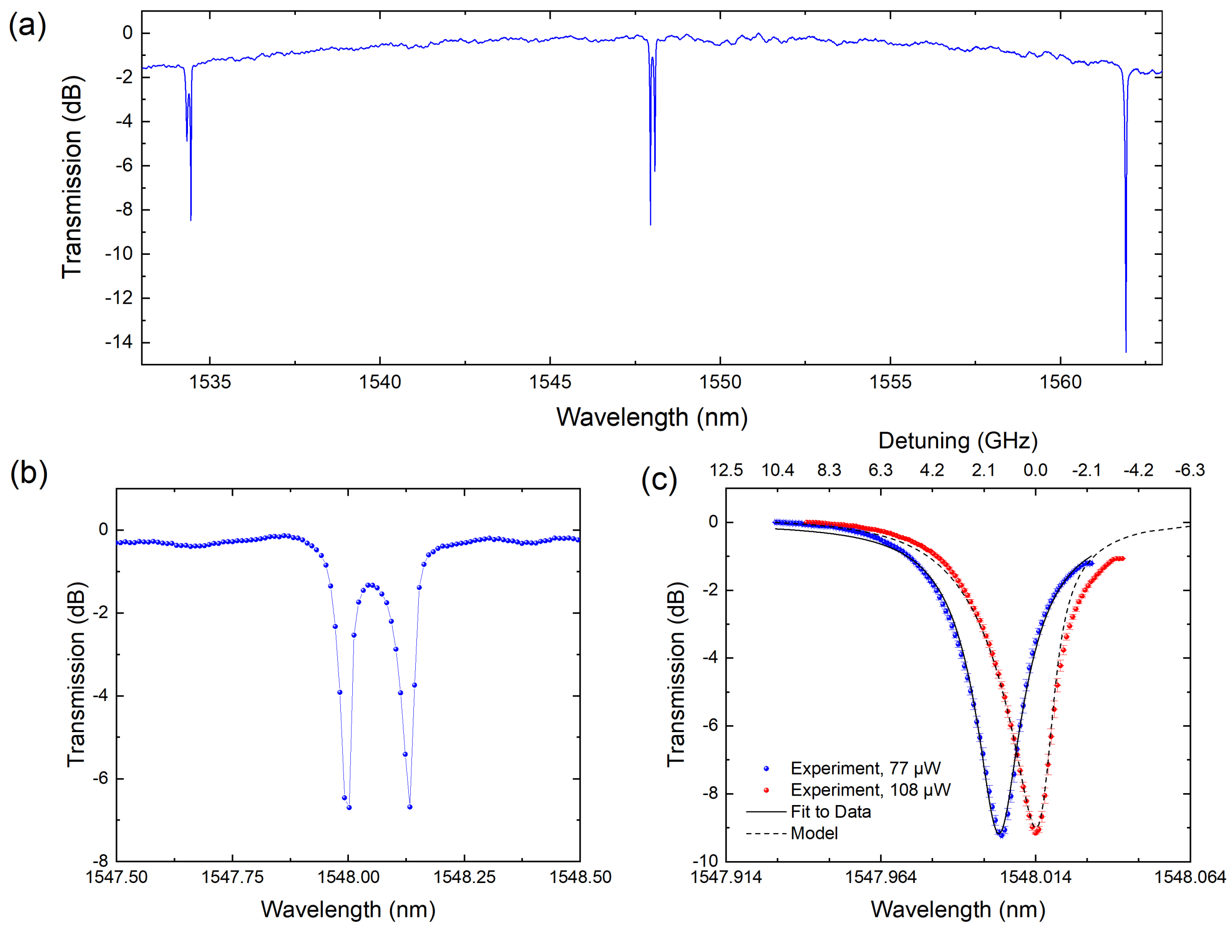

FIG. 3. (a) Sweep of the optical cavity response over a wide wavelength range. Three resonances are observed. The two lowest wavelength resonances exhibit peak splitting, but the highest wavelength response has no splitting and shows good extinction. For the following experiments, the probe is set to the side of the slope in the middle cavity. The pump is set to the bottom of the third resonance unless stated otherwise. (b) Coarse sweep of the probe optical cavity. Peak splitting is observed. (c) Fine sweep of the probe optical cavity at 77 μW (blue circles) and the corresponding curve fit (solid line). The experimental cavity data does not reach 0 dB on the red side because of the peak splitting. A second sweep at 108 μW (red circles) is also shown, with a theoretical model approximating the behaviour of the optical cavity (dashed line). The input probe laser power (in mW) is converted to find power at the bus waveguide (in μW) considering 65 percent losses.

TABLE II. List of pump optical cavity properties ($\lambda \approx$ 1560 nm)

Parameter	Value	Unit
$a_{\rm rt}$	0.9934	-
τ	0.9902	-
$\gamma/2\pi$	4.17	GHz
$\gamma_{\rm ex}/2\pi$	2.80	GHz
$P_{\rm bus,DC}$	258.2	μW
$P_{\rm bus,AC}$	34.4	μW
$\omega_0/2\pi$	192.2	THz

TABLE III. List of pump optical cavity properties ($\lambda \approx$ 1535 nm)

Parameter	Value	Unit
$a_{\rm rt}$	0.9936	-
τ	0.9952	-
$\gamma/2\pi$	3.23	GHz
$\gamma_{\rm ex}/2\pi$	1.39	GHz
$P_{\rm bus,DC}$	170	μW
$P_{\rm bus,AC,minimum}$ (Simulation)	1.13	μW
$P_{\rm bus,AC,maximum}$ (Simulation)	22.7	μW
$\omega_0/2\pi$	195.8	THz

the cantilever as 48 fg (1 fg= 10^{-15}g). We can also determine the noise floor of the system, which in turn can be used to establish the bottom of the dynamic range of the sensor [1, 20]. This noise floor is established by the thermomechanical noise of the cantilever, which has a known amplitude noise on resonance of [1]

$$S_{\rm x,peak} = \frac{4k_{\rm B}TQ}{m_{\rm eff}\Omega_0^3}, \tag{7}$$

where $k_{\rm B}$ is the Boltzmann constant and T is temperature. The thermomechanical noise is measured by setting the pump laser modulation off and measuring the mechanical response with the lock-in amplifier. The result of this measurement can be seen in Figure 4, and is expressed in terms of the detuning from cavity resonance. In this case, the optical cavity resonance ω_0 is set to the bottom of the optical resonance curve at the higher power of 108 μW (red dots in Figure 3(c)). The data has been smoothed to reduce the vibrational amplitude noise introduced by the vacuum pump. From Figure 4, we can determine that centre mechanical resonance frequency is $\Omega_0 = 2\pi \times 21.1956$ rad MHz, which is the frequency at zero detuning where the optical spring effect vanishes. The observation of the thermomechanical noise shows that we can access the noise floor of our device even at large detunings where the mechanical transduction by the optical cavity is not efficient. The average quality factor of the measurements in Figure 4 is 10,000, and therefore we set the mechanical $Q = 10,000$.

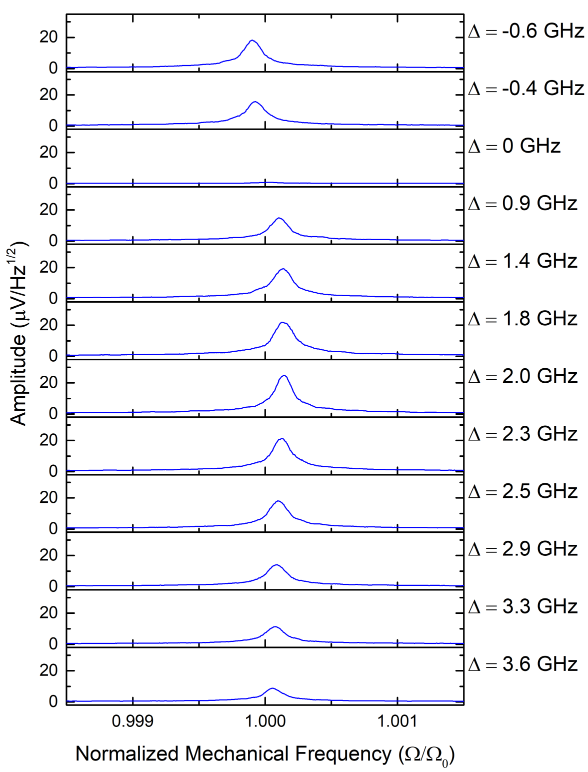

FIG. 4. Experimental measurement of the thermomechanical noise of the cantilever, smoothed to eliminate noise introduced by vacuum pump vibrations. This result can be used to extract the optomechanical coupling coefficient.

The final characterization is the optomechanical interaction. One of the most important parameters defining the optomechanical interaction is the optomechanical coupling coefficient $G = \partial\omega/\partial x$, which describes the strength of the interaction between the mechanical resonator and the optical cavity. There are several ways to determine the optomechanical coupling coefficient, one of which is by measuring the thermomechanical noise of the mechanical resonator at a variety of detunings. If the optomechanical coupling is sufficiently large, frequency shifts caused by the optical spring are observed. Since thermomechanical motions are small, the linearized version of the optomechanical equations can be used [22] which gives an expression for the optomechanical spring effect in the Doppler regime in terms of G. Thus the frequency shifts can be used to calculate the optomechanical coupling [17]. From Figure 4, we can extract the peak frequency of the mechanical response at each detuning and use this to calculate the optomechanical coupling coefficient. The resulting value is $G/2\pi = 0.157$ GHz/nm. The mechanical properties of the system are summarized in Table IV.

TABLE IV. List of mechanical properties

Parameter	Value	Unit
$G/2\pi$	0.157	GHz/nm
$\Omega_0/2\pi$	21.1956	MHz
Q	10,000	-
m_{eff}	47.7	fg
$S_{\text{x,peak}}$	1.2	pm/Hz$^{1/2}$

With the optical, mechanical, and optomechanical properties of the system without a driving force known, we can introduce the pump laser to provide actuation through the optical gradient force. This increases the complexity of the system, due to large amplitude nonlinearity, as we will see in the following section.

V. LARGE AMPLITUDE NONLINEARITIES

A. Red Stiffening and Blue Softening

To characterize the nonlinear behaviour of the optomechanical system using a pump-and-probe actuation and detection approach, we gradually increase the applied AC optical force and measure the mechanical amplitude response. We set the pump laser wavelength to the lowest point of the first optical resonance in Figure 3(a), and therefore the values listed in Table III apply. We activate our amplitude electro-optic modulator (EOM) and use the lock-in amplifier to increase the voltage applied to the EOM, thereby increasing the AC amplitude of the actuation power applied to the cantilever. The probe laser was positioned at the point of maximum slope on both the red and blue side of the optical cavity transmission from Figure 3(c), to maximize the signal-to-noise ratio of the mechanical signal. This corresponds to a detuning of approximately ±0.61 GHz. The lock-in amplifier was used to sweep the frequency of the voltage drive across the mechanical frequency spectrum to obtain driven measurements of the mechanical device. As the applied AC optical force was increased, nonlinearity was observed for both red and blue detuning. A stiffening nonlinearity was observed in the red-detuned measurements, whereas a softening nonlinearity was observed in the blue-detuned measurements (Fig. 5). This is opposite to the behaviour described by the optical spring effect in a typical optomechanical system. We will investigate the cause of this result in Section V F.

B. Readout Nonlinearity and Thermomechanical Calibration

To estimate the mechanical amplitudes in Fig. 5 (labeled "apparent amplitude"), one can use a detuning dependent conversion factor for voltage signal response to displacement by inspection of the thermomechanical peaks in Fig. 4. However, as pointed out in Section II, amplitudes derived in this way are inaccurate for large displacements due to readout nonlinearity. This can be confirmed with an estimation of the driving force. The optical gradient force acting on a mechanical device external to the optical cavity can be described mathematically by Eq. (8) and is a function of the laser detuning from the cavity resonance Δ [35].

$$F(x) = -\frac{2P_{\mathrm{bus}}\gamma_{\mathrm{ex}}G}{\omega(\Delta^2+\gamma^2)}, \tag{8}$$

All of these parameters are known experimentally from the measured optical cavity responses. Within or near the linear region, the force calculated from this expression can be used to estimate a corresponding amplitude using the simple relation for a damped harmonic oscillator, $F_{\mathrm{opt}} = kx/Q$, where $k = m_{\mathrm{eff}}\Omega_0^2$ is the spring constant, x is the amplitude, and Q is the quality factor. These values are known from the characterization of the mechanical device in the previous section. Using these well-known relationships, we can estimate that the largest amplitude in Figure 5(b) should be 6.3 nm. The largest amplitude in Figure 5(a) should be 20.7 nm (a larger voltage was applied to the red side). The expected amplitudes are a factor of 2.5–4.5 times larger than the apparent amplitudes due to the large amplitude readout nonlinearity. If motion is approximately 10 nm, as implied by estimate of the force, this represents a frequency modulation on the cavity resonance curve (via G) of approximately 2 GHz. This is comparable to the cavity linewidth, so it follows that the voltage output should have readout nonlinearities from large oscillations of the cavity resonance [18] as conceptualized in Section II.

C. Connecting Readout Harmonics With Cavity Resonance Shape

To obtain more information about the driven optomechanical system and large amplitude nonlinearities, we can perform a sweep of the mechanical signal at different detuning points in the optical cavity. We move the pump laser to the highest wavelength optical resonance in Figure 3(a), to improve the efficiency of the driving laser power by moving it to a non-backscattered peak. It also eliminates any possibility that the drive laser could shift from one minimum of the split cavity to the next, since the highest wavelength optical resonance does not exhibit any peak splitting. The pump laser power was set to a DC value of $P_{\mathrm{bus,pump}} = 258$ μW. A constant voltage of 200 mV was applied to the EOM, producing an AC power of 34 μW in the bus waveguide. The probe laser was activated and set to $P_{\mathrm{bus,probe}} = 108$ μW. Next, the probe laser wavelength was swept through the optical cavity, starting at the far blue-detuned side and increasing the wavelength to sweep through the cavity. At each wavelength position, the frequency response of the cantilever was measured using the lock-in amplifier. The frequency response at the fundamental resonance frequency was recorded, as well as data from higher harmonics ($2\Omega/2\pi$, $3\Omega/2\pi$, and $4\Omega/2\pi$).

The results of these sweeps are shown in Figure 6 and evidence of both readout and force nonlinearities are present. There are clear signals at all of the higher harmonics measured, which is indicative of a readout nonlinearity [11]. Also, a softening effect appears as the probe laser wavelength approaches the cavity centre from the blue side in Figure 6(e). A stiffening effect is visible as the probe laser wavelength moves past zero detuning and onto the red side 6(g). These effects are consistent with Figure 5, and are not observed in other reports of nonlinearities caused purely by readout [36–38]. From this result, we confirm that there are at least two sources of nonlinearity present in the system; a readout nonlinearity and a Duffing type nonlinearity.

To confirm that the harmonic components observed in Figure 6 are caused by a readout nonlinearity, and not another source of nonlinearity that induces higher order harmonics such as second-order optomechanical coupling [11], the relationship between the harmonics and the optical cavity is examined. If the optomechanical nonlinearity observed is caused mainly by a nonlinearity in the transduction, the shape of the optical cavity and its derivatives will correspond to the peaks of the harmonics observed in Figure 6. The voltage peaks are extracted from Figure 6 for the first and second harmonic, then normalized to one. The normalized values are plotted versus the detuning. The voltages where the mechanical phase is shifted by π are denoted as negative voltages. The result of this calculation is shown in Figure 7, where the fundamental peaks are represented by the blue circles, and the second harmonic peaks are represented by the red circles. We can then compare these curves to the derivatives of the nonlinear optical cavity model shown by the dashed line in Figure 3(c) and plotting the results versus the detuning. The first and second derivatives are shown in Figure 7 and are represented by the blue and red dashed lines, respectively.

The derivatives represent the slope and curvature of the cavity at an instantaneous point along the optical res-

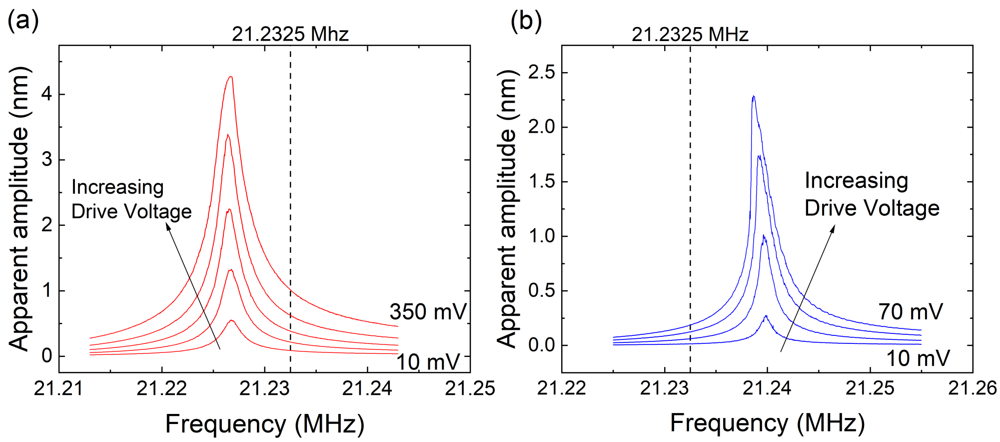

FIG. 5. The frequency response of the cantilever in apparent nanometres as the driving voltage is increased with the probe laser positioned on the (a) red and (b) blue sides of the optical cavity. The apparent amplitude is calculated using the thermomechanical noise calibration and assumes there is no readout nonlinearity. The power of the probe laser in the bus waveguide is 154 μW. The DC power of the pump laser in the bus waveguide is 170 μW. For (a), the AC optical power is increased from 1.13 μW to 39.7 μW. For (b), the AC optical power is increased from 1.13 μW to 7.93 μW. The pump laser frequency is held constant for both measurements. When the probe laser is positioned on the blue side, a softening effect is observed. When the probe laser is positioned on the red side, a stiffening effect is observed. This is opposite to the expected result in optomechanical systems.

onance curve. However, the large-amplitude cantilever in this experiment samples significantly more than a single point during one period of vibration. The optical cavity slope may be an accurate measure of the transduction for small amplitude vibrations such as the thermomechanical noise or doubly clamped beams [32, 39], but this does not hold for a driven cantilever where the amplitudes are large enough to move past the approximately linear section of the Lorentzian optical resonance. To more accurately map the slope and curvature that the cantilever samples as it moves through one period of vibration with a large amplitude, we take a moving average of the first and second derivatives of the optical cavity. The window size of this moving average is the peak-to-peak amplitude of the nanomechanical device converted to a detuning using the optomechanical coupling coefficient. The peak amplitude is estimated from observing the detuning at which the dips in the mechanical spectrum appear in Figure 6(f), since those dips arise from the probe laser crossing over the optical cavity resonance minimum, resulting in a change in slope and an abrupt change in the signal [18, 40]. We can use the first detuning that exhibits a dip and the last detuning without a dip as reference points to estimate the amplitude of the cantilever, and therefore also the window size for the integration [18]. At the detuning where the first dip occurs, we know that the optical cavity is moving from its initial detuning position to the other side of the optical cavity slope. This gives a minimum shift that the optical cavity is experiencing at the cantilever's peak amplitude. On the other hand, at the detuning immediately before the first dip, the probe laser does not complete the shift to the other side of the optical cavity. This detuning value gives a maximum amount of shift that the optical cavity is experiencing during the peak of the cantilever's vibration. By averaging the maximum and minimum shifts, we can obtain an estimate of the appropriate window size for the integration. The average shift is a substantial 1.95 GHz at the cantilever's peak amplitude. Therefore, the window for the integration should be twice this value, 3.9 GHz, to account for the peak-to-peak amplitude of the cantilever. To confirm that this estimate makes sense, we can convert the average shift to an amplitude using the optomechanical coupling coefficient $G = \partial\omega/\partial x \approx \Delta\omega/\Delta x$. The resulting amplitude is 12.3 ± 0.4 nm at $\Delta/2\pi = 2$ GHz, which is close to the expected amplitude of 11.0 nm given the optical force applied (Eq. (8)) during the experiment at $\Delta/2\pi = 2$ GHz.

The result of applying a 3.9 GHz wide moving average window to the first and second derivatives of the optical cavity is shown by the solid blue and red lines respectively in Figure 7. These curves agree very well to the peaks obtained from the mechanical sweeps for the first and second harmonics shown by the circles in Figure 7. This close agreement shows that the shape of the optical cavity is closely linked to the harmonics observed in the mechanical frequency spectrum. This is a strong indicator that the harmonics we have observed in the experiment are caused mainly by a readout nonlinearity, which is purely due to the nonlinear nature of the Lorentzian transfer function of the optical cavity. The nonlinear signal also confirms our understanding as to why the amplitude calculated using the thermomechanical noise responsivity (Figure 5) underestimated the actual amplitude: much of the energy of the driven signal is shifted from the fundamental resonance frequency to

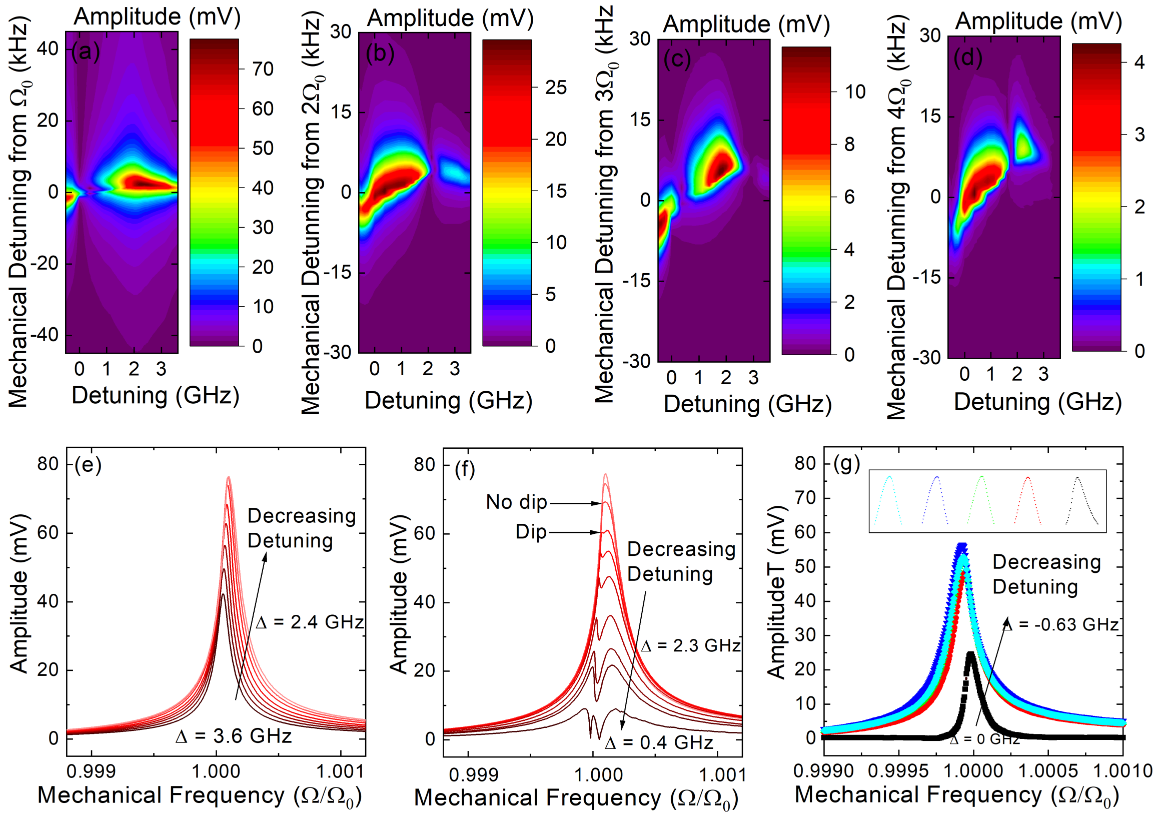

FIG. 6. The frequency response of the cantilever as the probe laser is swept through the optical cavity. In the bus waveguide, the probe power is 108 μW, the DC pump power is 258 μW, and the AC pump power is 34 μW. (a) The response at the fundamental resonance frequency. The black arrows show the peak height trend as the detuning is decreased. (b)–(d) The harmonic components at $2\Omega/2\pi$, $3\Omega/2\pi$, and $4\Omega/2\pi$, respectively. The harmonics are indicative of a readout nonlinearity. (e)–(g) The fundamental response is re-plotted to show the changing nonlinearity as the detuning is decreased. In (e), little nonlinearity or slight softening is observed for large positive (blue) detuning. In (f), as the detuning approaches zero, a clearer softening nonlinearity is observed and the peaks begin to have dips. The last peak without a dip is at $\Delta/2\pi = 2.0$ GHz and the first peak with a dip is at $\Delta/2\pi = 1.88$ GHz. The frequency difference between these peaks (i.e. $\Delta/2\pi = 2$) and $\Delta/2\pi = 0$ can be used to estimate that the amplitude is 12.3 ± 0.4 nm. In (g), the nonlinearity switches from softening to stiffening for detuning changing from zero to negative values. In (g inset) five peaks indicate the shape of peaks changes with detuning. From left to right, the detuning values of the inset plots are: -0.63 GHz, -0.50 GHz, -0.38 GHz, -0.25 GHz, 0 GHz, respectively.

the higher order harmonics. Calculating the amplitude using the thermomechanical responsivity does not take this energy loss and nonlinearity into account. Rather, to establish an absolute calibration of the displacement and transfer function, a full quantitative analysis of all harmonics, like that in Ref. [41] for a Fabry-Perot cavity, would need to be undertaken.

Although the cause of the harmonics in the mechanical frequency spectrum is a readout nonlinearity resulting from the Lorentzian shape of the optical cavity, the mechanical resonances in Figures 5 and 6(e) show softening and stiffening distortions that are similar to a Duffing nonlinearity. A readout nonlinearity alone is insufficient to explain these nonlinear effects. In the following sections, the other sources of nonlinearity in the optomechanical system are examined. Since driving the devices to high amplitude is crucial to reaching a high dynamic range for our mass sensing cantilevers, the understanding of other factors affecting the nonlinear behaviour of the system is essential.

D. Observed Optomechanical Force Nonlinearity

Figures 5 and 6 exhibit Duffing nonlinearities that we anticipate are caused by the optical force as laid out in Section II. Understanding and finding null points for this effect is crucial for maximizing the linear amplitude of the devices and ultimately their dynamic range for the benefit of their sensing properties. To experimentally determine the detuning with minimum nonlinearity, we examined the sweep data points near the peaks at the detunings where data looked most symmetrical. This is shown in Figure 6(g) and inset and reveals that the zero crossing of nonlinearity occurs somewhere between detunings of zero and -0.5 GHz. The ability to accurately model the location of zero crossing, given a set of experimental parameters, would allow design of the

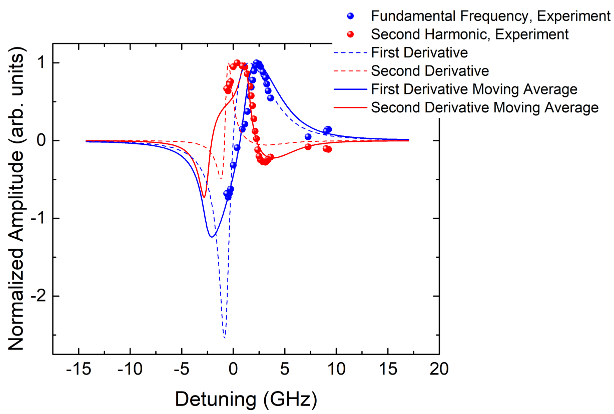

FIG. 7. The peak value of the mechanical signal is shown for the fundamental frequency (blue circles) and second harmonic (red circles). These peaks are extracted from Figure 6(a) and (b). The first (blue) and second (red) derivatives of the nonlinear optical cavity are shown by the dashed lines. A moving average of the first (blue) and second (red) derivatives with a window size equal to the peak-to-peak amplitude of the nanomechanical cantilever is shown by the solid lines. There is excellent agreement between the experimental peaks and the moving average of the first and second derivatives. This demonstrates that the harmonics in the mechanical frequency spectrum are directly related to the shape of the optical cavity and are a result of a readout nonlinearity. The large window of the moving average indicates that the readout is also directly affected by the large amplitude of the cantilever.

crossing at optimal points, e.g. at points of highest responsivity. An analytical model for the optomechanical nonlinearity caused by the optical force of a single laser was introduced in [16]. Without the inclusion of a second laser, however, the sign of the nonlinearity reported there tended to be opposite to the data presented here. An analytical model which took into account the forces from two lasers was reported in [18]. This model was successful in reproducing the observations of positive nonlinearity on the red side of the cavity and negative nonlinearity on the blue side, however, was only able to find nonlinearity zero crossings on the blue side. We turn to a numerical model to best reproduce the experimental data observed and to most accurately find the minimum nonlinearity detuning.

E. Two Contributions To Optomechanical Force Nonlinearity

From results of the numerical modeling (see next Section V F) we discern that it is crucial to include the optomechanical coupling coefficient dependence on displacement in order to reproduce the observed detuning ranges of softening and stiffening effects. We thus consider a division of the optical force nonlinearity into two components: nonlinearity introduced by the Lorentzian form of the optical cavity force, and nonlinearity introduced by the exponential decay of the evanescent field outside of the waveguide. The first type of optical force nonlinearity is a function of detuning, since the optical force applied will vary with the detuning according to Eq. (8). The second type of nonlinearity is relevant for optomechanical devices where the optical cavity is physically separated from the mechanical resonator, as in our case since the cantilever is adjacent to the racetrack resonator. For clarity, these different sources of nonlinear optical force are labeled as the optical cavity force nonlinearity and the evanescent force nonlinearity, respectively. The evanescent force strongly depends on the gap between the optical cavity and the mechanical element, and for larger gaps will be linear over a larger range.

Typically, the amplitudes of the cantilevers are sufficiently small that the exponential force can be linearized about the initial displacement point of the beam (that is, G is constant). In this case, however, the amplitudes are very large, and it turns out that the exponential form of the evanescent field must be accounted for. The optomechanical coupling has been previously demonstrated to have an exponential form [16], and can be written as

$$G = G_0 \exp(-2\zeta x), \tag{9}$$

where G_0 is the optomechanical coupling of the stationary device, x is the amplitude of the mechanical device, and ζ is the exponential decay constant of the evanescent field outside the waveguide. x is referenced to the initial, stationary position of the cantilever and is permitted to be positive or negative in the simulations. ζ is the same value previously calculated to be $1/83\ \mathrm{nm}^{-1}$ using mode solver simulations.

F. Numerical Model Of Optomechanical Force Nonlinearity

We have demonstrated that existing models of optomechanical nonlinearities do not sufficiently describe our optomechanical system, likely due to the complexity of the second pump laser in the system and the large amplitudes achieved by the cantilever using the pump-and-probe technique. The analytical approach in [16] was modified to account for the second laser in [13]. The new analytical model was able to qualitatively reproduce the positive red-shifted nonlinearity at -0.63 GHz detuning and the negative blue-shifted nonlinearity at +0.63 GHz detuning, but was not able to catch the correct nonlinearity sign over the whole detuning range. Here, to accurately model the behaviour of our optomechanical system we use a numerical approach. We solve a set of coupled differential equations that describe the interaction between the probe laser optical resonance, the pump laser optical resonance, and the mechanical resonator. This approach is derived using the energy coupling formalism for the optical cavity. The energy coupling formalism describes the coupling of optical power in time, and therefore we describe the evolution of the optical cavity amplitude as a function of time, $a(t)$. To describe the rate of change of the optical cavity amplitude as the mechanical device oscillates, we can use the optomechanical Hamiltonians. This procedure has been previously presented for the interaction between a mechanical resonator and a single optical cavity [22]. The additional complication in our system arises due to the presence of the pump laser to drive the nanomechanical device. The pump laser adds a second, time-varying optical cavity to the system of equations. By following the approach used in [22], we can write a system of equations for the optomechanical pump-and-probe system. The equations for the probe optical cavity (subscripts 1), pump optical cavity (subscripts 2), and mechanical resonators are as follows:

$$\dot{a}_1(t) = -\gamma_1 a_1(t) + i(\Delta_1 + Gx(t))a_1(t) + \sqrt{2\gamma_{\mathrm{ex},1} P_{\mathrm{bus},1}/\hbar\omega_1}, \tag{10}$$

$$\dot{a}_2(t) = -\gamma_2 a_2(t) + i(\Delta_2 + Gx(t))a_2(t) + \sqrt{2\gamma_{\mathrm{ex},2} P_{\mathrm{bus},2}/\hbar\omega_2}, \tag{11}$$

$$m_{\mathrm{eff}}[\ddot{x}(t) + \Omega_0 \dot{x}(t)/Q + \Omega_0^2 x(t)] = \hbar G|a_1(t)|^2 + \hbar G|a_2(t)|^2, \tag{12}$$

where $a(t)$ is the normalized (unitless) time-dependent optical cavity amplitude, and all other parameters have been previously defined. The main difference between Eqs. (10) and (11) are the functional forms of P_{in}, the input power to the system. $P_{\mathrm{in},1}$ is a DC optical power determined by the probe laser power input to the system, and the detuning Δ_1 varies to mimic the probe laser sweep in Figure 6. The pump input power, $P_{\mathrm{in},2}$, has both a DC and an AC component, to mimic the experimental conditions provided by the EOM. The form of the pump power is $P_{\mathrm{in},2} = P_{\mathrm{in},2}^{\mathrm{DC}} + P_{\mathrm{in},2}^{\mathrm{AC}} \cos(\xi\Omega_0 t)$. The pump laser has a constant detuning of $\Delta_2/2\pi = 0$ GHz, as it is always set at the cavity minima. The probe and pump input powers have both been normalized by $\hbar\omega$ such that the units for the input power are in Hz. The variable ξ is used to calculate the response off-resonance, and is defined as Ω/Ω_0. By setting ξ to a range of values between $\xi = 0.999$ and $\xi = 1.001$, the mechanical frequency in the equations can be effectively swept, thereby mimicking the experimental results. The model can also turn on or off the evanescent force nonlinearity by letting G either be constant or have the form of Eq. (9). By simultaneously solving these three equations numerically for a range of values for Δ_1 and ξ, we can determine a solution for $x(t)$ and $a(t)$ at various optical detunings and mechanical frequencies close to resonance. The coupled set of equations is solved simultaneously for time steps increasing from 100 ns to 1 ms. Once the time domain results are obtained, they are transformed to the frequency domain using a numerical fast Fourier transform. We select only the steady state data from the end of the simulations for our analysis. The values input to the simulation are listed in Tables I, II, and IV.

We compare the simulated optical cavity data $a_1(t)$, which is the optical resonance in which the probe laser is positioned, to the experimentally obtained results. To make this comparison, we start with the simulated value $a_1(t)$, which is the normalized, time-averaged complex amplitude inside the racetrack resonator cavity. To convert this value to the optical power inside the bus waveguide, we must convert the amplitude from a normalized value to an optical amplitude by multiplying the amplitude by $(\hbar\omega_1)^{1/2}$. Then, the equation for the all-pass microring resonator can be re-written in terms of the input power and cavity amplitude to obtain

$$P_{\mathrm{out},1} = |\sqrt{P_{\mathrm{in},1}} - \sqrt{2\gamma_{\mathrm{ex},1}\hbar\omega}\, a_1(t)|^2, \tag{13}$$

where $P_{\mathrm{out},1}$ is the output power in the bus waveguide from the racetrack resonator and includes the signal at the fundamental resonance frequency, as well as all of the higher order harmonics. It also includes a DC component. The DC component is comprised of the DC output from the optical cavity in the absence of modulation, which is the typical output observed in Figure 3, and a DC signal formed from the self-beating of the harmonics, which downmixes to a DC signal. By taking the Fourier transform of $P_{\mathrm{out},1}$, we can filter out the DC component at 0 Hz. The Fourier transform also allows us to separate the simulated results by frequency, allowing for results at the fundamental frequency and all of the higher order harmonics. We extract the peaks from the frequency spectrum for each detuning, normalized mechanical frequency ξ, and at the first four harmonics in the frequency spectrum. These simulated results are presented in Figs. 8, 9, and 10 with the experimental results plotted in the same graphs for straightforward comparison. Results at the fundamental resonance frequency are shown in Figure 8 and for the second through fourth harmonics in Figure 9 and 10.

The simulated results (points and dashed lines) are compared to the experimental results (solid lines). We normalize the experimentally recorded frequencies by $\Omega_0 = 2\pi \times 21.1956$ MHz, which is the resonance frequency of the thermomechanical noise at zero detuning (Figure 4). In all cases, the simulation is able to accurately reproduce the sign of the nonlinearity (either stiffening or softening) as well as the general shape of the experimental curves. Notably, the signal at $\Delta/2\pi = 1.13$ GHz at the fundamental harmonic (Figure 8(c)) even qualitatively captures a slight dip in the response related to the nonlinear readout. This demonstrates the model is able to reproduce the experimental results well. The remaining discrepancies may be a result of the slight optical nonlinearity in the optical cavity and uncertainty in experimentally determining the detuning.

A strength of the simulation is that mechanical amplitude data x is directly available, in addition to the optical cavity amplitude. These data are shown in Figure 11 for four different detunings. Figure 11 (a) is simulated with no evanescent nonlinearity (constant G) while Fig-

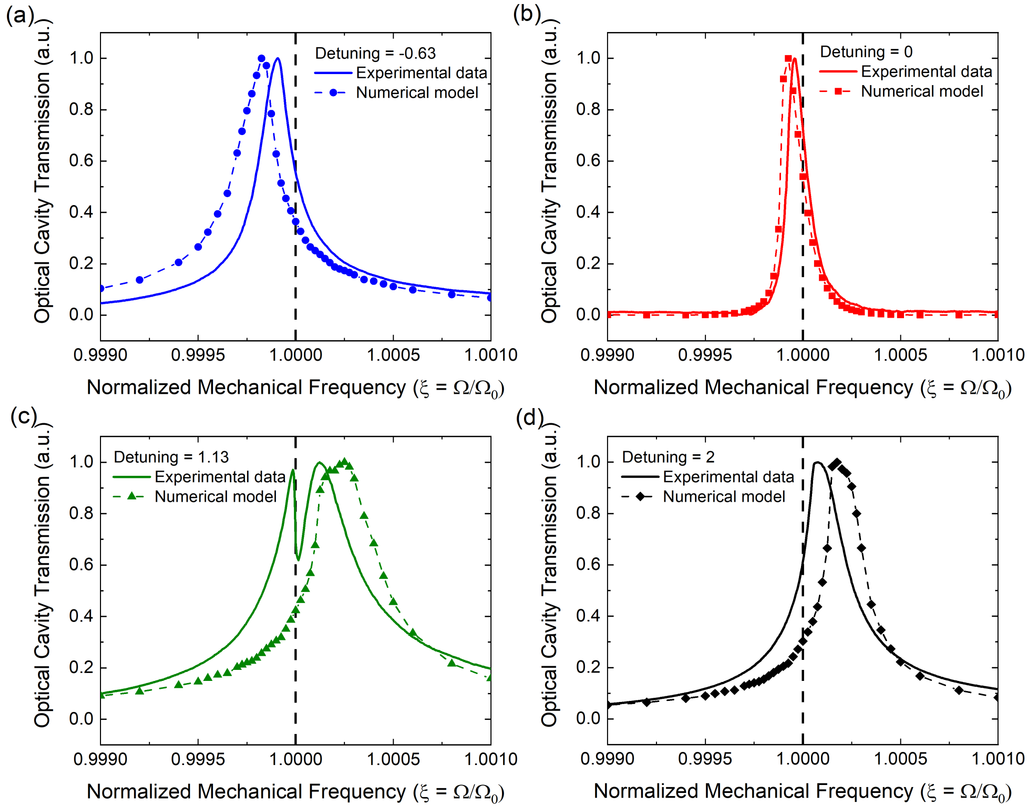

FIG. 8. Comparing the results from the numerical model (dashed lines with open symbols) to the experimental data (solid lines) for the fundamental mechanical resonance frequency, where the model includes a displacement-dependent G caused by the evanescent force. Values for detuning are (a) $\Delta/2\pi = -0.63$ GHz, (b) $\Delta/2\pi = 0$ GHz, (c) $\Delta/2\pi = 1.13$ GHz, and (d) $\Delta/2\pi = 2$ GHz. The correct stiffening and softening behaviour is identified by the numerical model for each detuning. The simulated peak shapes agree well with the experimental shapes, including at zero detuning. The slight dip in the result at $\Delta/2\pi = 1.13$ GHz is also predicted by the simulation. The difference in the size of the dip may be explained by the asymmetry in the optical cavity, which is not modeled by these simulations. Overall the agreement between the experimental and predicted peak shapes is excellent, and indicates that we have successfully modeled the sources of nonlinearity in the model.

ure 11 (b) includes the evanescent nonlinearity (Eq. 9). The calculated mechanical displacement had components only at the fundamental resonance frequency and no signals at higher frequency components, confirming that the harmonics are generated by the readout and not by the mechanical device itself. The same analysis procedure used to extract the frequency components of the simulated optical cavity data was used to extract the mechanical amplitude. The steady state time domain data was Fourier-transformed to frequency data, and the peak value extracted at each Δ and ξ. As expected, the simulated results report significantly higher amplitudes of the nanomechanical cantilever in comparison to the thermomechanical responsivity calibrated amplitudes of Fig. 5 which are compromised by the readout harmonics. The peak simulated amplitudes range from 12 nm at a detuning of $\Delta/2\pi = \pm 0.63$ GHz, up to a maximum of 13 nm at a detuning of $\Delta/2\pi = 2.0$ GHz. These amplitudes are very close to the 12.3 ± 0.4 nm estimated from Figure 6 and help confirm the estimation method. The peak heights of the simulations are as expected based on the optical damping and amplification. The amplitude of the cantilever measured by a red-detuned probe laser is slightly damped compared to the amplitude measured by a blue-detuned probe laser.

The main difference between the results in Figures 11 (a) and 11 (b) is that the mechanical signal at zero detuning exhibits softening in the latter figure. This is because of the extra nonlinearity included in this simulation, caused by the exponential form of the evanescent force. Including the evanescent nonlinearity is crucial to more closely match the observed transition between softening and stiffening in the experiment at slight negative detunings, rather than symmetrically around zero detuning. Comparison can be made to Fig. 6(g) and inset where the linearity can be seen to change from negative to positive in moving from zero detuning to -0.63 GHz.

The result obtained in Figure 11 is also important because it demonstrates that the amplitude of the mechanical signal does not change significantly throughout the range of detunings. The change in the amplitude between detunings in Figure 11 is less than 10%. The opti-

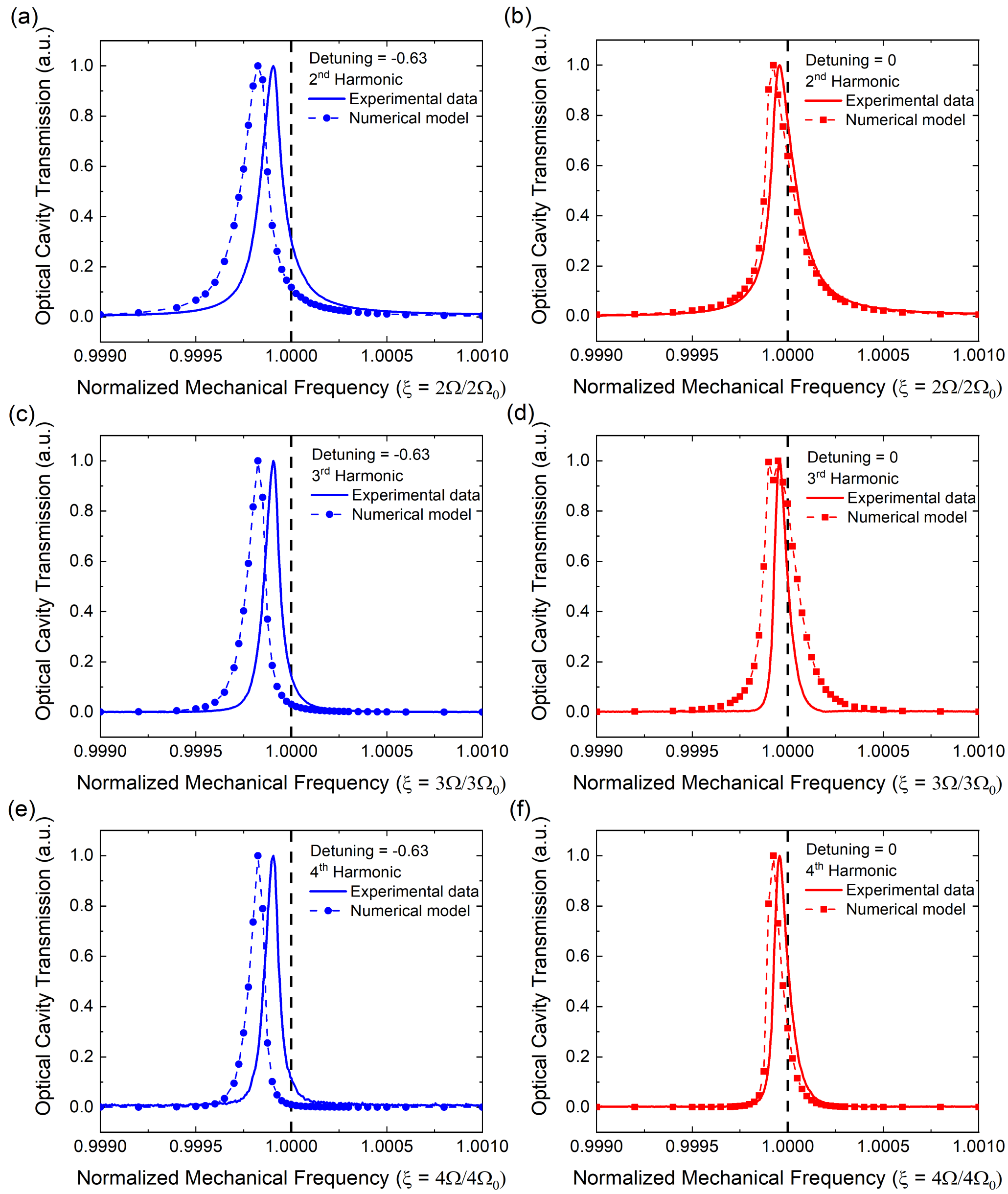

FIG. 9. Comparing the numerically modeled results (dashed lines with open symbols) to the experimental data (solid lines) for the second, third, and fourth harmonics, where the model includes a displacement-dependent G caused by the evanescent force. The results for $2\pi = -0.63$ GHz are shown for (a) the second harmonic, (c) the third harmonic, and (e) the fourth harmonic. The results for $\Delta/2\pi = 0$ GHz are shown for (b) the second harmonic, (d) the third harmonic, and (f) the fourth harmonic. The correct directions for the stiffening and softening are predicted for all detunings.

cal force nonlinearities induced by the pump and probe lasers clearly alter the peak shape and the nonlinear behaviour of the optomechanical signal, but do not substantially alter the amplitude of the mechanical device over the simulated detuning range. This indicates that the assumption that we made to calculate the moving average of the optical cavity derivatives in Figure 7 holds true; that is, using a window of constant size to calculate the moving averages is a reasonable approximation. Since the agreement between the optical cavity derivatives and the peaks of mechanical signals depends only on the window size, as demonstrated in Figure 7, we can conclude that the nonlinearity introduced by the probe laser does not substantially affect the harmonic content of the mechanical signal. In other words, the amplitude of the harmonics observed in the experiment are indeed purely a readout nonlinearity, and are not strongly affected by the optical force nonlinearity present in the system.

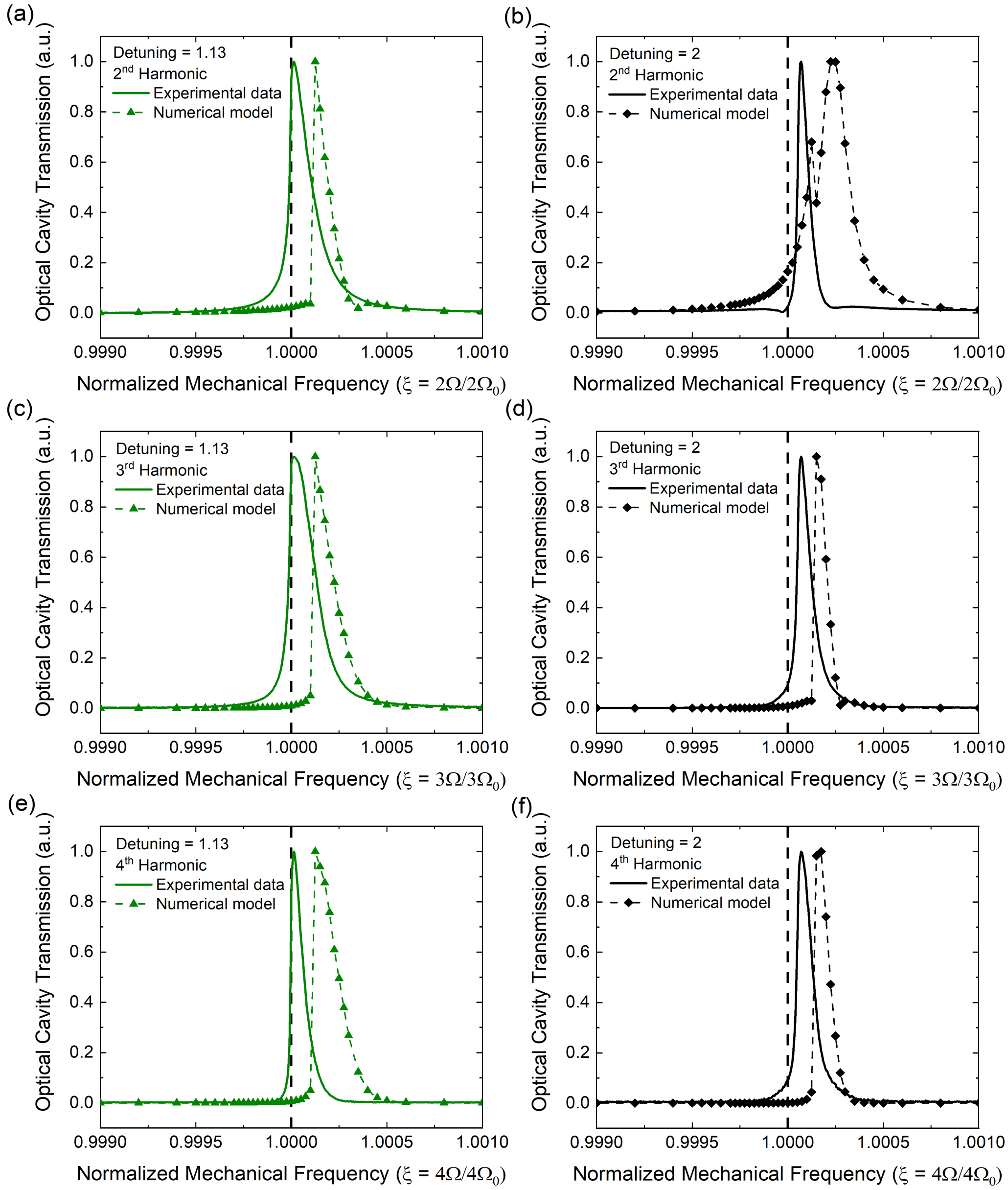

FIG. 10. Comparing the numerically modeled results (dashed lines with open symbols) to the experimental data (solid lines) for the second, third, and fourth harmonics, where the model includes a displacement-dependent G caused by the evanescent force. The results for $\Delta/2\pi = 1.13$ GHz are shown for (a) the second harmonic, (c) the third harmonic, and (e) the fourth harmonic. The results for $\Delta/2\pi = 2$ GHz are shown for (b) the second harmonic, (d) the third harmonic, and (f) the fourth harmonic. The correct directions for the stiffening and softening are predicted for all detunings.

G. Simulating the Critical Amplitude

The swept frequency modeling output can also be used to simulate the nonlinearity and critical amplitude as a function of probe laser detuning. By varying the AC component of $P_{\text{in},2}$ in the model, the drive power can be varied similarly to the experimental procedure of Figure 5. We perform these computations at detunings ranging from $\Delta/2\pi = -0.63$ GHz to 0 GHz. In fact, inspection of Fig. 11(b) and Fig. 6(g) allows us to choose a finer range of simulated detunings to try and find a minimum in the absolute value of optomechanical nonlinearity. For each drive power, the peak mechanical amplitude coordinate of the mechanical frequency sweep is extracted (both its frequency and amplitude). These coordinate points for all drive powers are combined on an amplitude vs frequency plot and repeated for detunings (a) -0.63 GHz, (b) 0 GHz, (c) -0.37 GHz, (d) -0.35 GHz, (e) -0.33 GHz, and (f) -0.31 GHz in Figure 12.

The nonlinearity value and critical amplitude are ex-

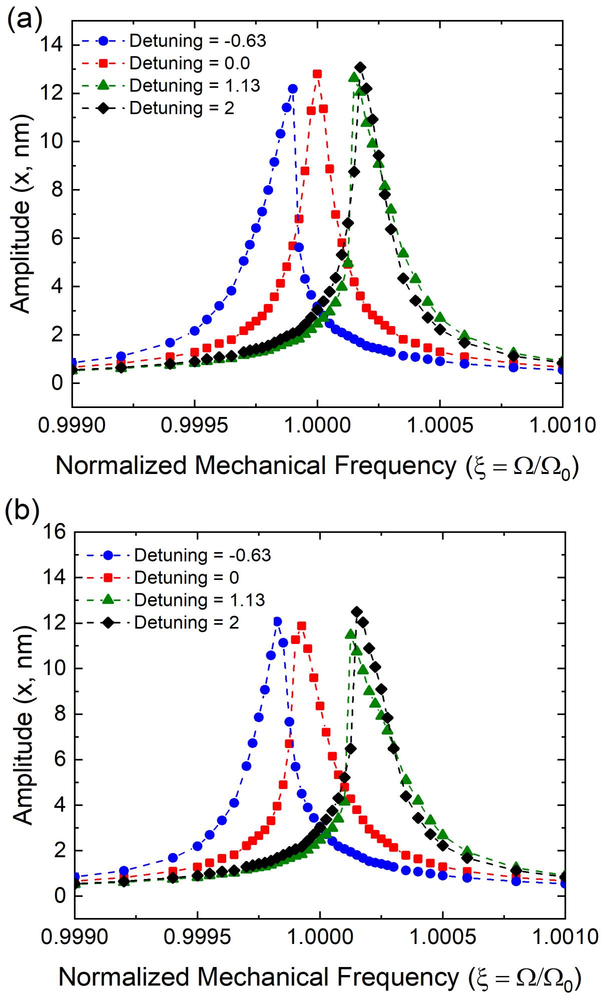

FIG. 11. Calculated amplitudes obtained from simultaneous solutions of Eqs. (10)–(12) (a) without and (b) with the exponential form of the optomechanical coupling included. The dashed lines are a guide to the eye. The importance of including the exponential optomechanical coupling is verfied by the zero detuning case which in (a) shows no nonlinearity while in (b) shows a softening nonlinearity: the latter is consistent with the experimental observations.

tracted using the "backbone" approach detailed in Section III. The curves in Figure 12 are fit using Eq. (4) to obtain the nonlinearity coefficient α. Finally, we input α into Eq. (2) to calculate the critical amplitude for each detuning. Critical amplitude and α are presented in Figure 12(h) as a function of detuning. Figure 12(g) displays the data from parts (a)-(f) on a single frequency axis for visual comparison of the leaning backbones. The more vertically aligned the backbone, the lower the nonlinearity and higher the critical amplitude.

This procedure yields an estimation of the nonlinearity null position in detuning at around -0.37 which produces a large value of critical amplitude near 70 nm. This is over four times larger than the critical amplitude of about 15 nm at the -0.63 GHz detuning, where the sensor would have been typically operated, and provides a substantial improvement of the system dynamic range. With thermomechanical noise floor (*cf.* Table IV) of 1.2 pm/Hz$^{1/2}$, this allows accessible signal to noise ratio (in a 1 Hz bandwidth) of $58,000$ vs. $12,000$ and dynamic range of 95 vs. 82 for $\Delta/2\pi = -0.37$ GHz vs. -0.65 GHz, respectively. Note that the noise floor is still experimentally resolved near -0.37 GHz detuning, so this detuning could be used for sensing with no detrimental effect of a lower responsivity. Furthermore, critical amplitude of 70 nm is far enough below the gap size of 90 nm to keep atomic force effects between cantilever and waveguide negligible. Thus, this dynamic range should be immediately reachable in the present experiment. The mass sensitivity level is defined as $\delta m = -2m_{eff}/(2Q\ SNR)$ which implies a sensitivity of 83 yg/Hz$^{1/2}$ associated with the optimal detuning near zero nonlinearity.

VI. DISCUSSION

In optomechanical systems undergoing large mechanical motion, complicated signals and dynamics exist arising from readout transduction and optomechanical force nonlinearities. Here, we have multiple simultaneous nonlinearities; readout nonlinearity, optical cavity force nonlinearity, and evanescent force nonlinearity. Without numerical modeling, we would not be able to separate them. With the modeling, however, we are able to confirm that the harmonics in the mechanical frequency spectrum are generated by the readout nonlinearity. This is caused by the Lorentzian lineshape of the optical cavity. The readout nonlinearity prevents proper calibration using the thermomechanical noise. The softening and stiffening behaviour observed in the experiment are a result of the optomechanical force nonlinearities, the optical cavity force nonlinearity caused by the pump and probe lasers moving through the Lorentzian lineshape of the optomechanical force curve and the evanescent force nonlinearity caused by the cantilever moving towards and away from the racetrack resonator. Inclusion of both is crucial for matching to experimentally observed nonlinearity at all detunings and allow for precisely identifying a null location in the nonlinearity for sensor improvement. Finally, our detailed numerical approach is important to ensure that the effects of both the pump and probe are modeled accurately. Previously published models studying optomechanical nonlinearities do not include a strong, amplitude modulated pump laser. Since the power of this laser is high, it is important that the optical force nonlinearities generated by this laser are taken into consideration as well. Table V summarizes different approaches used to model the optomechanical nonlinearity in the literature. This table demonstrates that our numerical model occupies a unique niche. It is the only model that accounts for nonlinearities using a pump-and-probe approach with an AC amplitude modulation on the pump laser.

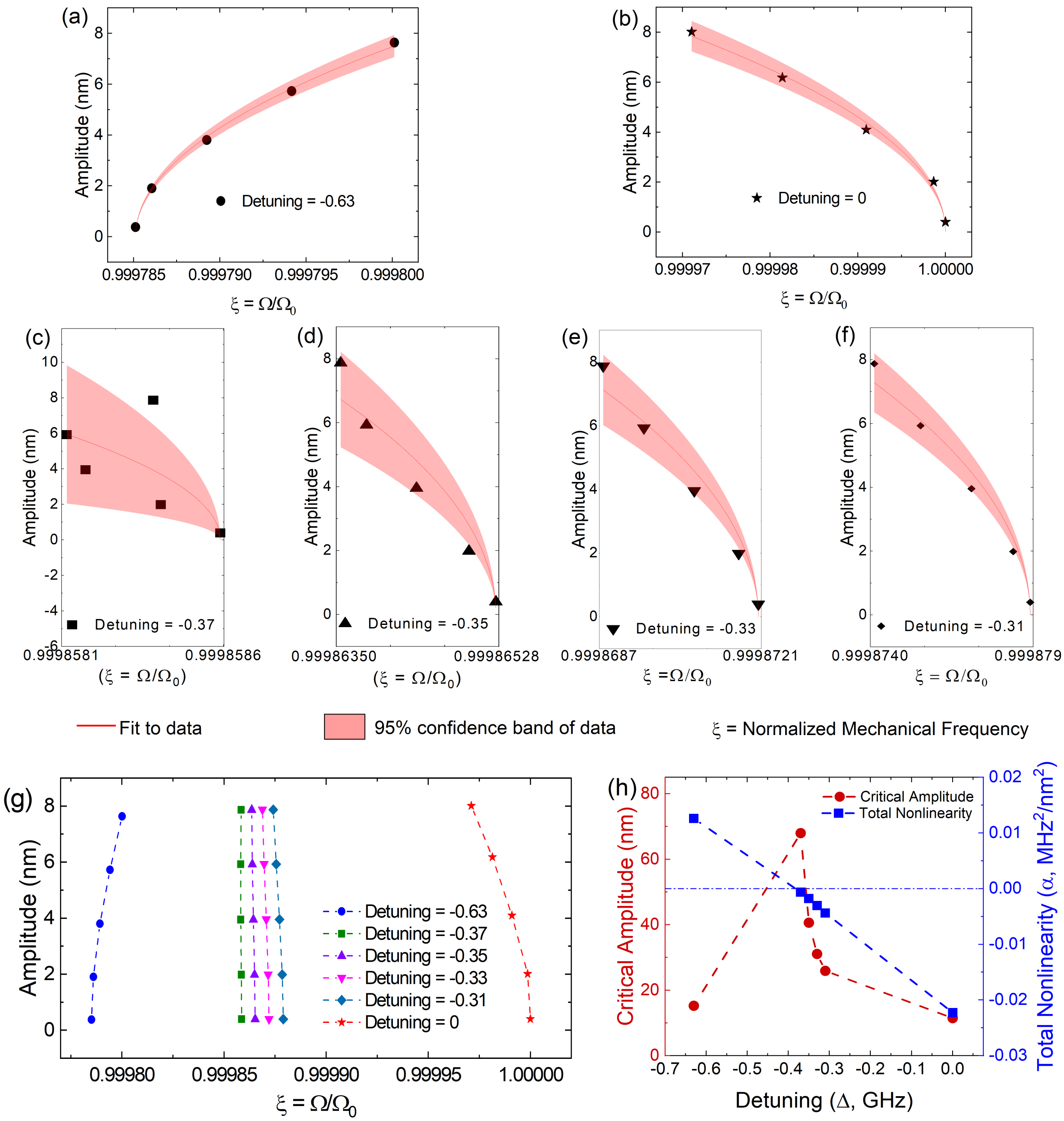

FIG. 12. **New description is needed for this figure.**(a) Modeled amplitudes with increasing input AC pump power. The optical cavity data input to the simulation were the same as the experimental results in Figure 5; the pump laser was positioned at the lowest-wavelength optical cavity resonance (Table III) Nope not true - the pump is on the highest wavelength resonance, and the probe laser was positioned at the point of steepest slope on the centre optical cavity transmission. (b) Critical amplitude extraction using the backbone curve technique for the blue side model. The critical amplitude is 5.8 nm. (c) Critical amplitude extraction using the backbone technique for the red side model. The critical amplitude is 6.3 nm. The simulated result that the critical amplitude is larger for red probe detuning compared to blue probe detuning matches the experimentally observed result in Figure 5.

By comparing the information from experiments and the detailed numerical modeling with and without the exponential form of the optomechanical coupling included, we are able to fully understand the source of nonlinearities in our optomechanical system. This is important so that we can design future optomechanical systems for reduced nonlinearity to improve the dynamic range of our sensor. To reduce the readout nonlinearity, we can design optical cavities with longer linear ranges or smaller optomechanical coupling. Smaller optomechanical coupling

TABLE V. Summary of Approaches to Optomechanical Nonlinearity

Type of Nonlinearity	Experiment	Bessel Function Expansion [12]	Optical Force Expansion [16]	Numerical Model, Constant G	Numerical Model, Exponential G
Readout	Yes	Yes	No	Yes	Yes
Optical cavity force, DC	Yes	Yes	Yes	Yes	Yes
Evanescent force, DC	Yes	No	Yes	No	Yes
Optical cavity force, AC	Yes	No	No	Yes	Yes
Evanescent force, AC	Yes	No	No	No	Yes

will result in a smaller optical cavity shift for a given nanomechanical amplitude. To reduce the optical cavity force nonlinearity, the optomechanical coupling could be reduced, or the optical input power could be reduced. The detuning is also an important point to choose experimentally, as the detuning impacts the amount of nonlinearity caused by the optical cavity force. Reducing optomechanical coupling could also reduce the evanescent force nonlinearity, so that the operation point of the optomechanical system is in the more linear region of the exponential curve. Clearly, a higher optomechanical coupling is not necessarily ideal for optomechanical systems to be used as mass sensors. The downside of decreasing the optomechanical coupling is a decrease in the responsivity and the efficiency of the optical driving force, as the readout and actuation are both proportional to the optomechanical coupling.

Clearly many possibilities exist to improving the dynamic range of the optomechanical system. A trade-off in the design can optimize both the linearity of the system and the signal to noise ratio. With the knowledge of the source of the nonlinearity, and the ability to simulate the different types of nonlinearity individually, we can determine the best designs to maximize both the linear range and the detuning with minimum nonlinearity while maintaining a suitable signal to noise ratio.

VII. CONCLUSION

We have demonstrated that several optomechanical nonlinearities occur simultaneously when a mechanical device such as a cantilever is undergoing large amplitude vibrations induced by a coherent driving force. The nano-optomechanical pump-and-probe system produces harmonics in the mechanical frequency spectrum, which are a signature of a readout nonlinearity. The system also exhibits a stiffening nonlinearity when the probe is red-detuned and a softening nonlinearity when the probe laser is blue detuned, which is opposite to the typical result introduced by the optical spring effect. These nonlinearities are caused by an optical cavity force nonlinearity induced by the detuning of the probe laser in the system. The third nonlinearity, caused by the evanescent force outside of the racetrack resonator cavity, results in a signal at zero detuning that exhibits a softening nonlinearity. These types of nonlinearity cannot be separated and understood only by looking at the experimental results or by previous models in the literature due to the added complexity of the pump laser in the system. We have used full numerical modeling to study the system and determine the differences between these two sources of nonlinearity. The numerical models also aid in the determination of the mechanical amplitude, since the typical thermomechanical noise responsivity cannot be used to calibrate the amplitude when the readout is nonlinear.

Numerical modeling of our pump-and-probe optomechanical system provides a much better understanding of the dynamics of the system, and allows us to separate the readout nonlinearity from the two optical force nonlinearities. In the future, these results could allow for better optical cavity design for optimization of linear operation for both the force and the transduction. The full understanding of the nonlinearities in the system may also be useful for applications where nonlinearities are required, and in determining whether a sensor is in the linear or nonlinear regime.

VIII. ACKNOWLEDGMENTS

This work was supported by the National Research Council of Canada's Nanotechnology Research Centre (NANO) and its fabrication, microscopy, and characterization facilities. It was also supported by the Natural Sciences and Engineering Research Council of Canada, the Vanier Canada Graduate scholarship program (J. N. W. -B.), and by Alberta Innovates. Device fabrication was facilitated through CMC Microsystems (silicon photonics services and CAD tools) with postprocessing at the University of Alberta nanoFAB. Equations were solved numerically by using GNU Octave [**?**].

[1] Swapan K Roy, Vincent T K Sauer, Jocelyn N Westwood-Bachman, Anandram Venkatasubramanian, and Wayne K Hiebert. IMProving mechanical sensor performance through larger damping. *Science*,

360(6394):eaar5220, 2018.

[2] N Kacem, J Arcamone, F Perez-Murano, and S Hentz. Dynamic range enhancement of nonlinear nanomechanical resonant cantilevers for highly sensitive NEMS gas/mass sensor applications. *Journal of Micromechanics and Microengineering*, 20(4):45023, apr 2010.

[3] L G Villanueva, E Kenig, R B Karabalin, M H Matheny, Ron Lifshitz, M C Cross, and M L Roukes. Surpassing Fundamental Limits of Oscillators Using Nonlinear Resonators. *Phys. Rev. Lett.*, 110(17):177208, apr 2013.

[4] Xin You Lü, Jie Qiao Liao, Lin Tian, and Franco Nori. Steady-state mechanical squeezing in an optomechanical system via Duffing nonlinearity. *Phys. Rev. A*, 91(1):1–7, 2015.

[5] Changyao Chen, Damian H Zanette, Jeffrey R Guest, David A Czaplewski, and Daniel Lopez. Self-Sustained Micromechanical Oscillator with Linear Feedback. *Phys. Rev. Lett.*, 117(1):1–5, 2016.

[6] S Krylov, B R Ilic, D Schreiber, S Seretensky, and H G Craighead. The pull-in behavior of electrostatically actuated bistable microstructures. *J. Micromechanics Microengineering*, 18(5):55026, may 2008.

[7] I Kozinsky, H W C Postma, I Bargatin, and M L Roukes. Tuning nonlinearity, dynamic range, and frequency of nanomechanical resonators. *Appl. Phys. Lett.*, 88(25):1–4, 2006.

[8] King Yan Fong, Linran Fan, Liang Jiang, Xu Han, and Hong X Tang. Microwave-assisted coherent and nonlinear control in cavity piezo-optomechanical systems. *Phys. Rev. A*, 90(5):1–5, 2014.

[9] Florian Marquardt, J G E Harris, and S M Girvin. Dynamical multistability induced by radiation pressure in high-finesse micromechanical optical cavities. *Phys. Rev. Lett.*, 96(10):1–4, 2006.

[10] Fenfei Liu, Seyedhamidreza Alaie, Zayd C Leseman, and Mani Hossein-Zadeh. Sub-pg mass sensing and measurement with an optomechanical oscillator. *Opt. Express*, 21(17):19555–19567, 2013.

[11] C Doolin, B D Hauer, P H Kim, A J R MacDonald, H Ramp, and J P Davis. Nonlinear optomechanics in the stationary regime. *Phys. Rev. A*, 89(5):1–6, 2014.

[12] Alex G Krause, Jeff T Hill, Max Ludwig, Amir H Safavi-Naeini, Jasper Chan, Florian Marquardt, and Oskar Painter. Nonlinear Radiation Pressure Dynamics in an Optomechanical Crystal. *Phys. Rev. Lett.*, 115(23):1–5, 2015.

[13] Jocelyn N Westwood. *Improving the Performance of Nano-Optomechanical Systems for use as Mass Sensors.* PhD thesis, University of Alberta, 2018.

[14] Jack C Sankey, Cheng Yang, Benjamin M Zwickl, Andrew M Jayich, and Jack G E Harris. Strong and Tunable Nonlinear Optomechanical Coupling in a Low-Loss System. *Nat. Phys.*, 6(9):12, 2010.

[15] G A Brawley, M R Vanner, P E Larsen, S Schmid, A Boisen, and W P Bowen. Nonlinear optomechanical measurement of mechanical motion. *Nat. Commun.*, 7:10988, 2016.

[16] Huan Li, Yu Chen, Jong Noh, Semere Tadesse, and Mo Li. Multichannel cavity optomechanics for all-optical amplification of radio frequency signals. *Nat. Commun.*, 3:1091, 2012.

[17] M P Maksymowych, J N Westwood-Bachman, A Venkatasubramanian, and W K Hiebert. Optomechanical spring enhanced mass sensing. *Applied Physics Letters*, 115(10):101103, 2019.

[18] Jocelyn N Westwood-Bachman, Timothy S Lee, and Wayne K Hiebert. Efficient actuation design for optomechanical sensors. *Opt. Express*, 28(22):32349–32362, oct 2020.

[19] J N Westwood-Bachman, M P Maksymowych, V Van, and W K Hiebert. Transduction of large optomechanical amplitudes with racetrack-loaded Mach-Zehnder interferometers. *Opt. Express*, 28(15):21835–21844, jul 2020.

[20] K L Ekinci, Y T Yang, and M L Roukes. Ultimate limits to inertial mass sensing based upon nanoelectromechanical systems. *J. Appl. Phys.*, 95(5):2682–2689, 2004.

[21] N Kacem, S Hentz, D Pinto, B Reig, and V Nguyen. Nonlinear dynamics of nanomechanical beam resonators: improving the performance of NEMS-based sensors. *Nanotechnology*, 20(27):275501, jul 2009.

[22] Markus Aspelmeyer, Tobias J Kippenberg, and Florian Marquardt. Cavity optomechanics. *Rev. Mod. Phys.*, 86:1391–1452, 2014.

[23] V Van. *Optical Microring Resonators: Theory, Techniques, and Applications.* Taylor & Francis, 2017.

[24] Mani Hossein-Zadeh and Kerry J Vahala. Observation of optical spring effect in a microtoroidal optomechanical resonator. *Opt. Lett.*, 32(12):1611–1613, 2007.

[25] Mahmood Bagheri, Menno Poot, Mo Li, Wolfram P H Pernice, and Hong X Tang. Dynamic manipulation of nanomechanical resonators in the high-amplitude regime and non-volatile mechanical memory operation. *Nat. Nanotechnol.*, 6(11):726–732, 2011.

[26] Ali H Nayfeh, Mohammad I Younis, and Eihab M Abdel-Rahman. Dynamic pull-in phenomenon in MEMS resonators. *Nonlinear Dyn.*, 48(1-2):153–163, 2007.

[27] L G Villanueva, R B Karabalin, M H Matheny, D Chi, J E Sader, and M L Roukes. Nonlinearity in nanomechanical cantilevers. *Physical Review B - Condensed Matter and Materials Physics*, 87(2):24304, jan 2013.

[28] Ron Lifshitz and M C Cross. Nonlinear Dynamics of Nanomechanical and Micromechanical Resonators. In *Rev. Nonlinear Dyn. Complex.*, pages 1–52. 2009.

[29] Silvan Schmid, Luis Guillermo Villanueva, and Michael Lee Roukes. *Fundamentals of Nanomechanical Resonators.* Springer, 2016.

[30] J N Westwood-Bachman, Z Diao, V T K Sauer, D Bachman, and W K Hiebert. Even nanomechanical modes transduced by integrated photonics. *Appl. Phys. Lett.*, 108:61103, 2016.

[31] A H Nayfeh and D T Mook. *Nonlinear Oscillations.* Wiley Classics Library. Wiley, 2008.

[32] V T K Sauer, Z Diao, M R Freeman, and W K Hiebert. Optical racetrack resonator transduction of nanomechanical cantilevers. *Nanotechnology*, 25(5):55202, feb 2014.

[33] Lumerical Solutions Inc. Lumerical Solutions MODE.

[34] Cameron Horvath, Daniel Bachman, Rob Indoe, and Vien Van. Photothermal nonlinearity and optical bistability in a graphene-silicon waveguide resonator. *Opt. Lett.*, 38(23):5036–5039, dec 2013.

[35] Mo Li, Wolfram H P Pernice, and Hong X Tang. Reactive Cavity Optical Force on Microdisk-Coupled Nanomechanical Beam Waveguides. *Phys. Rev. Lett.*, 103(22):223901, nov 2009.

[36] H Rokhsari, T J Kippenberg, T Carmon, and K J Vahala. Radiation-pressure-driven micro-mechanical oscillator. *Opt. Express*, 13(14):5293, 2005.

[37] Fenfei Liu and Mani Hossein-Zadeh. Characterization of optomechanical rf frequency mixing/down-conversion and its application in photonic rf receivers. *J. Light. Technol.*, 32(2):309–317, 2014.

[38] Chenguang Huang, Jiahua Fan, Ruoyu Zhang, and Lin Zhu. Internal frequency mixing in a single optomechanical resonator. *Appl. Phys. Lett.*, 101(23):231112, 2012.

[39] Mo Li, W H P Pernice, C Xiong, T Baehr-Jones, M Hochberg, and H X Tang. Harnessing optical forces in integrated photonic circuits. *Nature*, 456:480–484, nov 2008.

[40] M Poot, K Y Fong, M Bagheri, W H P Pernice, and H X Tang. Backaction limits on self-sustained optomechanical oscillations. *Phys. Rev. A - At. Mol. Opt. Phys.*, 86(5):1–8, 2012.

[41] Roberto De Alba, Christopher B Wallin, Glenn Holland, Slava Krylov, and B Robert Ilic. Absolute deflection measurements in a micro- and nano-electromechanical Fabry-Perot interferometry system. *Journal of Applied Physics*, 126(1):14502, 2019.